Fiber-Interferometric Second Harmonic Generator with Dual-Color Standard Quantum-limited Noise Performance

MARVIN EDELMANN,[1,2,3,*] MIKHAIL PERGAMENT,[1] YI HUA,[4] MALEK M. SEDIGHEH,[1,2] AND FRANZ X. KÄRTNER[1,2,3,5]

[1]*Center for Free-Electron Laser Science CFEL, Deutsches Elektronen-Synchrotron DESY, Notkestr. 85, 22607 Hamburg, Germany*
[2]*Department of Physics, Universität Hamburg, Jungiusstr. 9, 20355 Hamburg, Germany*
[3]*Max Planck School of Photonics, Hans-Knöll-Straße 1, 07745 Jena, Germany*
[4]*Deutsches Elektronen-Synchrotron DESY, Notkestr. 85, 22607 Hamburg, Germany*
[5]*The Hamburg Center for Ultrafast Imaging, Luruper Chaussee 149, 22761 Hamburg, Germany*
**marvin.edelmann@desy.de*

Abstract: In this work, we present a novel fiber-interferometric device that achieves dual functionality: simultaneous amplification of a pulsed input signal and generation of its second harmonic while effectively suppressing the intensity noise in both modes, reaching the standard quantum-limit. The underlaying mechanism is based on phase-biased nonlinear polarization rotation coupled with type-I phase-matched second harmonic generation, a concept that is both theoretically investigated and experimentally verified. In the experiment, a fiber-optic system is constructed capable of generating 42 MHz ultra-low noise sub-150 fs output pulse trains simultaneously at 1030 nm and 515 nm, with average powers of 160 mW and 42 mW, respectively. Systematic frequency-resolved intensity noise measurements confirm dual wavelength, quantum-limited noise suppression beyond 100 kHz offset-frequency, with suppression levels up to 14 dB, showing correlation with local maxima in average power in both fundamental and second harmonic mode.

1. Introduction

The presence of fluctuations in ultrafast laser sources limits a wide range of applications in ultrafast science and technology, including multiphoton microscopy [1], photonic microwave generation [2], frequency metrology [3], and arbitrary waveform generation [4]. Extensive research over the last decades has focused on developing high-performance, i.e. ultra-low noise, laser systems. Fiber lasers have emerged as promising candidates due to their resilience against environmental disturbances, efficient heat dissipation, and high beam quality. Leveraging a versatile set of nonlinear effects, these lasers can further be tailored for specific applications. The ongoing evolution of ultra-low noise fiber oscillators, achieved through techniques like mode-locking via nonlinear interferometers (e.g., NALM/NOLM) [6-8] or self-stabilized fiber interferometers [9-11], now enables the generation of optical pulse trains with exceptional low intensity noise, timing jitter, phase noise, and frequency stability [12,13].

However, further adjustments of optical pulse trains beyond the capabilities of current state-of-the-art fiber oscillators in terms of average power, repetition rate, spectral bandwidth, or center wavelength while preserving their ultra-low noise characteristics frequently presents a formidable challenge. In terms of low noise optical amplification, significant strides have been made. Notably, the output power of inherently low-noise fiber oscillators has been vastly increased through specialty fibers [14-16] and intra-cavity divided pulse amplification [17,18]. Novel nonlinear amplifier schemes [19-21] and opto-electronic feedback mechanisms [22-24] further enable simultaneous power amplification, nonlinear spectral broadening, and

suppression of parameter fluctuations in the amplified optical pulse trains. With respect to a noise-less scaling of the pulse trains repetition-rate, Ying et al. recently showcased a GHz repetition rate fiber oscillator configuration with superior timing-jitter and relative intensity noise (RIN) characteristics [25]. In addition, recent efforts by Lacin et al. demonstrate a promising approach towards stability-enhanced harmonic mode-locking to reach the GHz regime without compromising laser noise performance [26]. Nonetheless, notable limitations in achieving ultra-low noise characteristics in optical pulse trains often arise due to nonlinear conversion processes such as second harmonic generation (SHG) and difference frequency generation (DFG). These mechanisms play a pivotal role for center wavelength shifts beyond the emission spectra of conventional laser gain materials and therefore have a significant impact e.g., in the fields of nonlinear biological imaging and spectroscopy as well as ultrafast quantum optics. While SHG for instance is theoretically able to suppress input fluctuations even beyond the standard quantum-limit (SQL) under certain conditions [27-30], the narrow parameter space and high requirements regarding system stability and alignment often not allow the successful implementation for many experimental setups. To the contrary, the vast majority of recent experimental studies report a strong amplification of the input RIN by up to 6 dB and a broadband increase in RIN spectral density, usually explained with the quadratic dependence of the SHG power stability on pump power fluctuations [31-35].

In a recent study, we demonstrated the immense potential of active nonlinear fiber-interferometers for simultaneous intensity noise suppression and signal amplification of arbitrary optical input pulse trains [19]. Expanding on this technology, this work introduces a novel, highly-flexible method for ultra-low noise SHG based on phase-biased Kerr-type fiber-optic nonlinear polarization rotation (NPR) in interaction with type-I phase-matched nonlinear crystals. The mechanism is theoretically described and experimentally implemented to construct a versatile fiber-optical system for the simultaneous ultra-low noise generation of directly compressed sub-150 fs optical pulse trains at 1030 nm and 515 nm with standard-quantum limited noise performance from an initially noisy input signal. Systematic measurements reveal a highly tunable access to operating points characterized by simultaneous convergence of local power transfer maxima and noise suppression in both operational modes—namely, the fundamental and second harmonic pulse trains, each emanating from separate output ports. Frequency-resolved RIN measurements validate more than 14 dB noise suppression in both modes and confirm the concurrent dual-color SQL noise performance. Up to 160 mW and 42 mW in the fundamental and second harmonic mode, respectively, are obtained at 43 MHz repetition rate.

2. Experimental setup and mechanism

We start our investigation by introducing the experimental setup and the underlaying mechanisms for ultra-low noise SHG. The experimental setup is shown in Fig.1 [a]. A home-built, Yb-doped ultrafast fiber laser generates linearly polarized optical pulses with a repetition rate of 43 MHz and a maximum output power of 150 mW, corresponding to a pulse energy of ~3.5 nJ. The inset in Fig.1 shows the measured spectrum and autocorrelation (AC) emitted by the laser source at full power. The spectral full width at half maximum (FWHM) is ~17.2 nm centered at 1032 nm. Assuming a Gaussian pulse shape, the FWHM of the positively chirped output pulse is ~4.6 ps. The half-wave plate HWP1 is rotated to ensure maximum transmission at PBS1. The generated output pulse train is directed into a module for type-I phase-matched SHG with a 3 mm long BBO crystal cut at an angle of 24.3°, a dichroic mirror (DM), and two BBAR-coated focusing lenses (Lens 1/2), each having a 19 mm focal length. In forward direction, HWP2 is set to rotate the polarization direction orthogonal to the phase-matched axis of the BBO, hence no SHG signal is generated at this point and the pulse train simply passes through the SHG module. It then propagates through a tunable phase-bias module, consisting

of an eight-wave plate (EWP, rotation angle $\boldsymbol{\theta_{\lambda/8}}$) and HWP3 (rotation angle $\boldsymbol{\theta_{\lambda/2}}$) in combination with a 45° Faraday-rotator (FR, single-pass) before entering a parallel transmission grating pair (GP, LightSmyth T-1000-1040 Series) with 1000 lines/mm grating constant in double pass configuration for tunable dispersion-management. The pulse train then enters a nonlinear and reflective fiber interferometer (NLI), which can be realized e.g., in configuration of a linear self-stabilized fiber interferometer (LSI) or a nonlinear amplifying loop mirror (NALM); both systems are currently often used by the research community as artificial saturable absorbers in ultra-low noise mode-locked fiber lasers [36-38]. The NLI fulfills the same dual functionality in both configurations; amplification of the input signal and accumulation of a nonlinear phase-difference $\boldsymbol{\Delta\varphi_{nl}}$ between two orthogonal polarization modes that propagate independently in the respective NLI arms, resulting in an intensity-dependent nonlinear polarization rotation (NPR). In the subsequent experiment, we decided to implement an LSI due to its straight-forward installation and alignment procedure, in particular with respect to the SHG module.

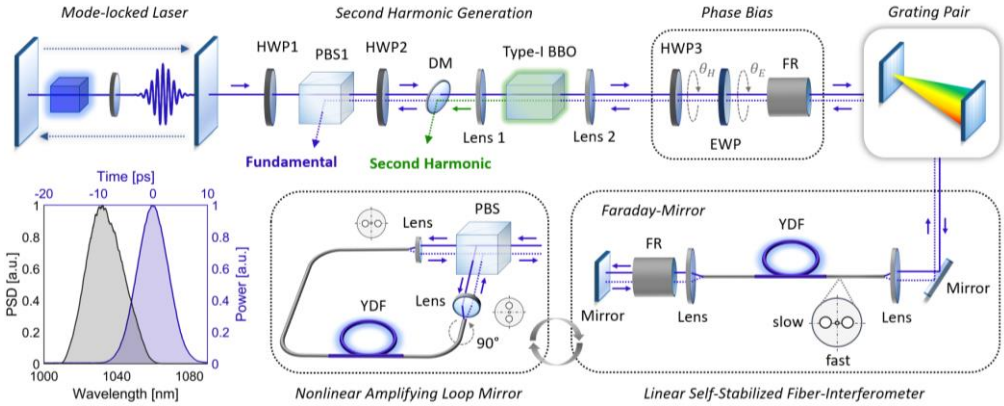

Fig. 1. Experimental setup of the fiber-interferometric second harmonic generator for the simultaneous generation of compressed pulse trains at 1030 nm and 515 nm with standard quantum-limited intensity noise. Inset: Measured spectrum (black) and autocorrelation trace (blue) of the mode-locked laser source with FWHM of ~24 nm and 6.7 ps, respectively. HWP, half-waveplate; PBS, polarization beam-splitter; DM, dichroic mirror; EWP, Eight-waveplate; FR, Faraday-rotator; YDF, Ytterbium-doped fiber.

The LSI is composed of an all-polarization maintaining fiber segment affixed to a fiber-coupled Faraday-rotator mirror (FRM). The 8 m fiber segment comprises 5 m of Yb-doped active fiber (YDF, Coherent PM-YSF-LO-HP), pumped by a 1 W laser diode emitting at 976 nm and a wavelength division multiplexer (WDM) and thus acts as a double-pass fiber amplifier. The slow axis of the PM-fiber is aligned to the reflection axis of PBS1 and to the phase-matched axis of the BBO. By adjusting phase-bias settings $\theta_{\lambda/8}$ and $\theta_{\lambda/2}$, two orthogonal polarization modes are generated from the initial linearly polarized input field that leaves PBS1. These modes couple to the fast and slow axes of the PM-fiber segment within the LSI. The evolution of these orthogonal polarization modes is influenced by the fiber's birefringence, leading to an independent propagation through the LSI at different group velocities, the accumulation of a differential nonlinear phase-shift $\Delta\varphi_{nl}$ due to the optical Kerr effect and a simultaneous amplification in the YDF. After a single pass, the Faraday-rotator mirror (FRM) rotates the polarization by 90° which counteracts the birefringent drift-off, causing the two amplified polarization modes to recombine upon double-pass through the LSI. A more detailed description of both the LSI and NALM working principle can be found in the literature e.g., in

Ref. [6,39]. The amplified and nonlinearly modulated LSI output field then proceeds along a trajectory back to the SHG module, having traversed once more through the GP and phase-bias. However, in contrast to the case of forward propagation in the SHG module, the LSI output pulses now have a component parallel to the phase-matched BBO axis resulting from the linear phase shift given by the phase-bias settings in conjunction with the nonlinear, intensity-dependent phase-shift determined by the magnitude of NPR in the LSI.

Due to the working principle of the LSI any peak power fluctuations $\bar{P}_{in}(t) + \delta P_{in}(t)$ present in the LSI input field E_{in}, where $\bar{P}_{in}(t)$ denotes the average power at time t and $\delta P_{in}(t)$ a time-variant noise term, are transferred to fluctuations of the differential nonlinear phase-shift $\Delta\varphi_{nl}$ according to the relation

$$\Delta\varphi_{nl}(t) = \overline{\Delta\varphi_{nl}}(t) + \delta\Delta\varphi_{nl}(t) = L_{LSI} n_2 g \frac{\pi}{\lambda_s A_{eff}} (\bar{P}_{in}[t] + \delta P_{in}[t])(2\varepsilon - 1) \qquad (1)$$

where λ_s denotes the center wavelength of E_{in}, A_{eff} the effective mode-field area in the LSI fiber segment, g the lumped gain factor of the LSI, n_2 the nonlinear refractive index, ε the energy splitting ratio between the orthogonal polarization modes and L_{LSI} the LSI fiber length [39,40]. To understand the resulting influence of the noise transfer at both the BBO and PBS1, one has to consider the relation of $\Delta\varphi_{nl}$ with the polarization state of the LSI output field E_{out}. To do so, it is convenient to express E_{out} arriving at the BBO as a Jones-vector in the form

$$\vec{E}_{out}(t) = \begin{pmatrix} E_{fast} exp\left\{-i\frac{(\Delta\varphi_{nl}(t) + \varphi_{pb})}{2}\right\} \\ E_{slow} exp\left\{i\frac{(\Delta\varphi_{nl}(t) + \varphi_{pb})}{2}\right\} \end{pmatrix} \qquad (2)$$

where $E_{fast} \approx \sqrt{(1-\varepsilon)g}E_{in}$ approximates the output electric field amplitude parallel to the fast axis of the LSI, $E_{slow} \approx \sqrt{\varepsilon g}E_{in}$ the amplitude parallel to the slow axis, $\Delta\varphi_{nl}$ the differential nonlinear phase shift and φ_{pb} the generalized phase-shift caused by the non-reciprocal phase-bias. To express $\vec{E}_{out}(t)$ with experimental phase-bias parameters (e.g., $\theta_{\lambda/8}$ and $\theta_{\lambda/2}$ for the setup in Fig.1), the Jones-formalism can be applied on the system as described in detail e.g., in Ref. [6,9,10]. Since both the phase-matched axis of the BBO and the reflection axis of PBS1 are aligned parallel to the slow axis of the LSI, the instantaneous rotation angle ξ(t) be determined by calculating the angle between $\vec{E}_{out}(t)$ and a unit vector $\vec{e}_{SHG,R} = \binom{0}{1}$ parallel to the respective axes. By further considering the inherent transfer of power fluctuations to fluctuations of $\Delta\varphi_{nl}$ in the LSI given by Eq. (1), one arrives at

$$\begin{aligned} \xi(t) = \bar{\xi}(t) + \delta\xi(t) &= cos^{-1}\left(\sqrt{\varepsilon}\, cos\left(\frac{\overline{\Delta\varphi_{nl}}(t) + \delta\Delta\varphi_{nl}(t) + \varphi_{pb}}{2}\right)\right) \\ &= cos^{-1}\left(\sqrt{\varepsilon}\, cos\left(\frac{\pi}{2\lambda_s A_{eff}} L_{LSI} n_2 g(\bar{P}_{in}(t) + \delta P_{in}(t))(2\varepsilon - 1)\right.\right. \\ &\quad \left.\left. + \frac{\varphi_{pb}}{2}\right)\right) \end{aligned} \qquad (3)$$

as an analytical expression for the transfer of power fluctuations at the LSI input to fluctuations of the instantaneous polarization angle $\xi(t)$ at the LSI output with respect to the relevant axes

for conversion efficiency/power transfer at the BBO and PBS1, respectively. If neglecting distortions in the SHG process caused by birefringent walk-off, dispersion and other crystal properties, the generated power in the second harmonic mode is $P_{SHG}(t) \propto \vartheta \cdot sin^2(\xi(t))$, where ϑ denotes the maximum achievable SHG efficiency. The reflected power emitted at PBS1, influenced by the prior SHG (Fig.1), scales with $P_R(t) \propto sin(\xi(t)) - \vartheta \cdot sin^2(\xi(t))$. By substituting Eq. (3) into those expressions, the noise transfer function for the second harmonic and fundamental output fields can be determined by taking the derivative dP_{SHG}/dP_{in} and dP_R/dP_{in}, respectively. For the purpose of generalization, it is convenient to express the power and noise transfer as function of $\Delta\varphi_{nl}$ instead of P_{in}; both parameters are directly proportional but $\Delta\varphi_{nl}$ further includes all system-specific LSI parameters and the gain factor of the LSI fiber amplifier according to Eq. (3). Consequently, the noise transfer for the second harmonic and fundamental reflected output mode, normalized to the experimental parameters and the LSI input power, can be described via $dP_{SHG}/d\Delta\varphi_{nl}$ and $dP_R/d\Delta\varphi_{nl}$, respectively. For system working points that result in $dP_R/d\Delta\varphi_{nl} \approx 0$, strong suppression of the input power fluctuations can be obtained.

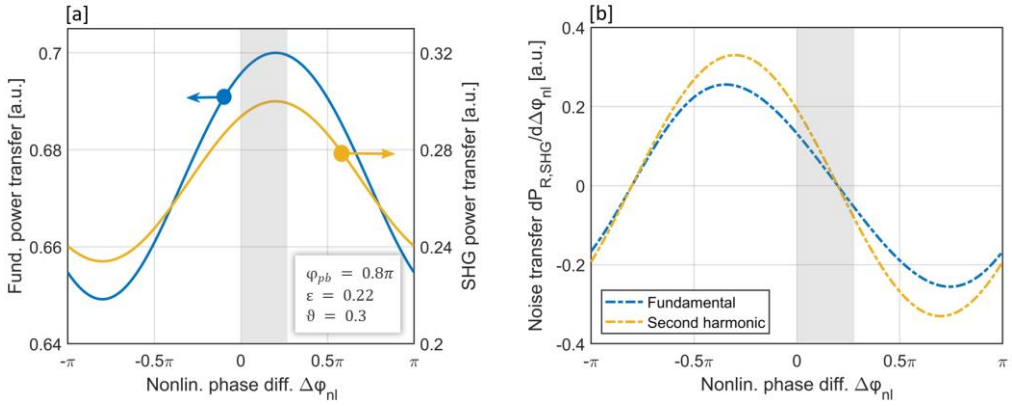

Fig. 2. [a]: Transfer functions of the amplified LSI output power $P_R/(gP_{in})$ and $P_{SHG}/(gP_{in})$ with $\varepsilon = 0.22$, $\varphi_{pb} = 0.8\pi$ and $\vartheta = 0.3$ as function of the accumulated nonlinear phase-difference $\Delta\varphi_{nl}$ to the fundamental (blue) and second harmonic (yellow) system output, respectively. [b]: Corresponding absolute noise transfer functions $dP_R/d\Delta\varphi_{nl}$ and $dP_{SHG}/d\Delta\varphi_{nl}$. The marked area highlights the operation range $0 \leq \overline{\Delta\varphi_{nl}}(t) \leq 0.3\pi$ enabling noise suppression with $dP_{SHG}/d\Delta\varphi_{nl} \approx 0$ for an exemplary pulse at the LSI input.

Fig.2 [a] shows the numerically obtained power transfer function for both operational modes in an arbitrary LSI with $\varepsilon = 0.75$ and $\varphi_{pb} = \pi$ as a function of the power-dependent $\Delta\varphi_{nl}$. Here, the output power $P_{R,SHG}$ is related to the LSI input power P_{in} amplified by the lumped LSI gain factor g. The corresponding noise transfer functions are shown in Fig.2 [b]. For an exemplary LSI output pulse where the intensity-dependent $\overline{\Delta\varphi_{nl}}(t)$ varies in the grey marked range between $0 \leq \overline{\Delta\varphi_{nl}}(t) \leq 0.3\pi$, the correct setting of ε and φ_{pb} via the phase-bias enables strong noise suppression around the peak of the exemplary pulse where $\overline{\Delta\varphi_{nl}}(t) \approx 0.3\pi$ with close to maximum power transfer in both operational output modes simultaneously. It is further shown, that the pure sin^2 dependence of the second harmonic signal results in a larger modulation depth of the noise transfer function.

3. Experimental results and discussion

As a first step of the experimental evaluation, the system performance is systematically investigated to confirm the theoretically predicted working points with simultaneous strong noise suppression and efficient power conversion in both fundamental mode (FM) at 1030 nm and the second harmonic mode (SHM) at 515 nm. Starting with an analysis of the systems dual-color power transfer, Fig.3 [a] and [b] show the measured average power in the FM and SHM at the respective output ports as function of the tunable phase-bias angle $\theta_{\lambda/8}$ with $\theta_{\lambda/2} = 160°$. The corresponding output spectra are shown in Fig.3 [c] and [d], respectively. All rotation angles are measured relative to the PBS reflection axis in mathematical standard convention. To ensure a precise comparison, $\theta_{\lambda/8}$ is electro-mechanically tuned with a digitally controlled rotation mount. In the experiment, the input pulse train is launched into the system with a pulse energy of ~0.75 nJ. The linear loss of the system, including SHG module, GP and LSI is estimated to be ~42%. To compensate this loss and further amplify the pulse energy while avoiding nonlinear distortions of the spectrum, the YDF in the LSI is optically pumped with 500 mW average power from the 976 nm laser diode. The grating distance of the GP is set to ~42 mm in order to compensate the chirp of the input pulse and the dispersion of the LSI fiber segment, thus ensuring a compressed pulse with maximum peak power in the SHG module.

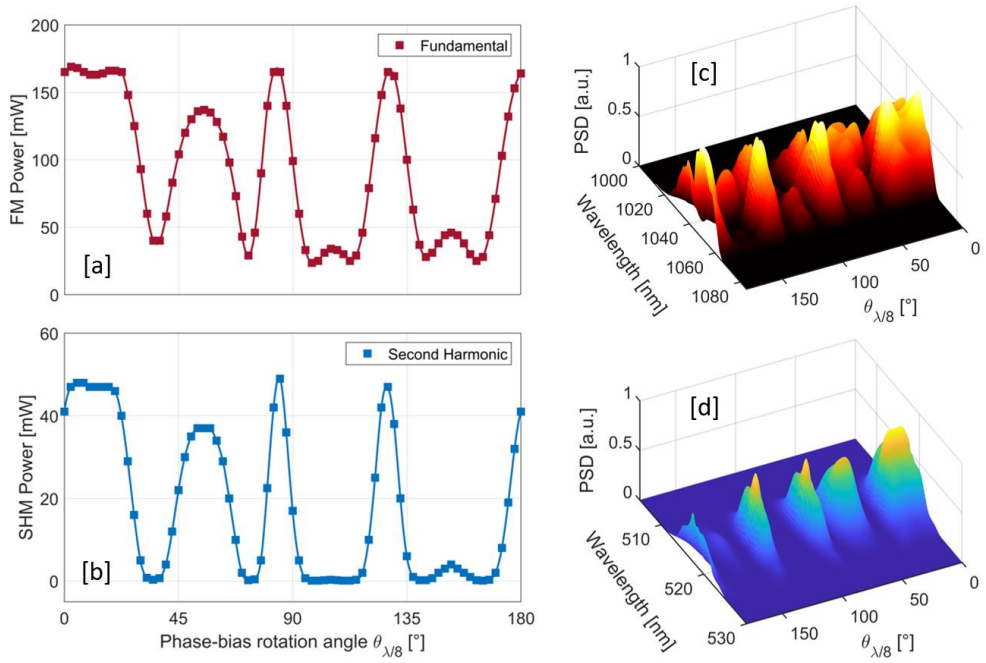

Fig. 3. [a]: Measured average output power of the 1030 nm FM of the LSI at the reflected PBS1 output port as function of the phase-bias rotation angle $\theta_{\lambda/8}$. [b]: Corresponding average power of the 515 nm SHM measured behind the DM. [c]: Measured LSI output spectra of the FM as function of $\theta_{\lambda/8}$. [d]: Corresponding SHM spectra.

In agreement with the theoretical prediction, the trend of the obtained power transfer between FM and SHM is directly related as consequence of the parallel alignment between PBS1 reflectance axis and phase-matched axis of the BBO. At an angle of $\theta_{\lambda/8} = 85°$, the maximum simultaneously obtainable output power in the FM and SHM is obtained with ~165 mW and ~50 mW corresponding to pulse energies of 3.8 nJ and ~1.2 nJ, respectively. The complex interplay between the energy splitting ratio ε between the PM-fiber axes in the LSI and the

phase-bias φ_{pb}, both coupled with the settings of $\theta_{\lambda/8}$ and $\theta_{\lambda/2}$, results in multiple of such local maxima in the measured power transfer curve.

In the next step, the correlation of the FM and SHM power transfer with the respective noise transfer is investigated. To this end, the relative intensity noise (RIN) spectra in both operational modes are measured as function of $\theta_{\lambda/8}$ with the same LSI parameters as before, and compared to the RIN spectrum of the LSI input generated by the laser source. In the laser source and the FM, the RIN spectra are measured as following. In a first step, the optical pulse train is detected with a fast and low-noise InGaAs photo-detector (Coherent, ET-3010). The 3rd harmonic at ~126 MHz of the obtained radio-frequency (RF) signal is then filtered with a proper bandpass-filter, and amplified with a low-noise trans-impedance amplifier (MiniCircuits ZX60-33LN-S+) driven by a highly stable power supply (Toellner TOE8721). The frequency-resolved RIN spectrum of the resulting RF-signal is then measured with a signal-source analyzer (SSA, Keysight E5052B) in a range from 1 kHz to 20 MHz. The lower limit of the bandwidth is set to exclude low frequency environmental noise contributions in the experiment, the upper limit results from bandwidth limitations of the RF-components.

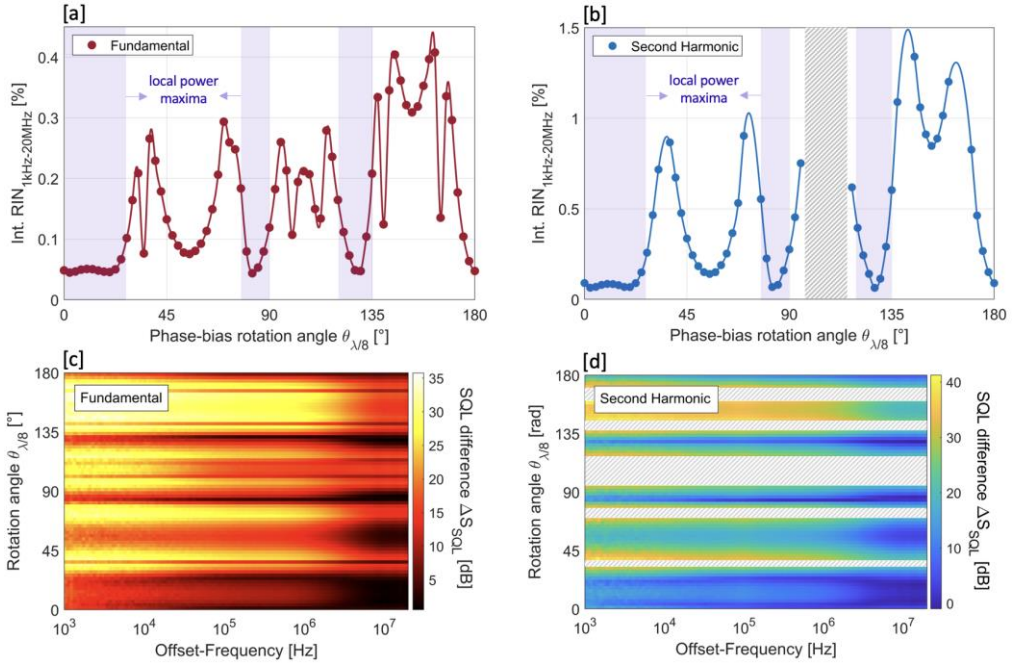

Fig. 4. [a]: Measured integrated RIN (1kHz-20MHz) of the FM as function of the phase-bias rotation angle $\theta_{\lambda/8}$. The violet marked areas corresponds to a local maximum in average power. [b]: Simultaneously measured integrated RIN of the SHM as function of $\theta_{\lambda/8}$. [c]: Frequency-resolved RIN spectra of the FM as function of $\theta_{\lambda/8}$. [d] Corresponding RIN spectra of the SHM. The shaded areas correspond to local power minima which prohibit RIN measurements.

The method to analyze the RIN of the SHM is in principle identical, with the exception that a biased Silicon photo-detector (Coherent, ET-2030) is used to efficiently detect at 515 nm center wavelength. The required usage of different detector schemes results in a different standard quantum-limit (SQL) for the RIN of both operational modes. For the FM and the laser source, an RMS voltage of 5 mV for the detected RF-signal in conjunction with 100 Ω termination and

a detector responsivity of 0.75 A/W results in a calculated SQL for the RIN at -142 dBc/Hz. In the case of the SHM, the measurements are conducted with an RMS voltage of 11 mV, a termination of 50 Ω and a responsivity of 0.25, resulting in a SQL for the RIN at -137.7 dBc/Hz. To ensure a consistent frame of reference, the SQL values in the respective modes are kept constant for all subsequent RIN measurements.

Fig.4 [a] and [b] show the RIN values obtained by integrating the measured RIN spectral densities over the full measurement bandwidth (1kHz to 20 MHz) for both the FM and SHM as function of the phase-bias angle $\theta_{\lambda/8}$. All other parameters are identical to the previous experiments. As shown, the area around $\theta_{\lambda/8} = 85°$ and range $0° \leq \theta_{\lambda/8} \leq 35°$ with local maxima in average power for both FM and SHM are correlated with local minimum values of the measured int. RIN in both modes. The RIN reaches down to 0.04% for the FM and 0.07% for the SHM. In further agreement with the theoretical evaluation, the RIN modulation depth for the SHM is significantly higher compared to the FM, which can be explained with the sin^2-dependence of its noise transfer. In addition, it can be seen that the overall structure of the RIN traces in both modes is closely related, which further verifies the theoretical trend. Fig.4 [c] and [d] show the corresponding frequency-resolved RIN spectra for FM and SHM respectively. To ensure comparability, the RIN spectral density is shown as SQL difference $\Delta S_{SQL,dB}(f) = S_{FM,SHM}(f) - S_{SQL\ (FM,SHM)}$, where f denotes the offset-frequency, S_{SQL} the frequency-independent SQL of the respective mode as calculated previously and $S_{FM,SHM}(f)$ the frequency-dependent output RIN spectral density measured with the SSA in FM or SHM. While the range of $0° \leq \theta_{\lambda/8} \leq 35°$ corresponds to a large plateau in maximum power and low noise for both modes, the area around $\theta_{\lambda/8} = 85°$ indicates lower values of $\Delta S_{SQL}(f)$, in particular also for the lower frequency range $f \leq 10^5\ Hz$.

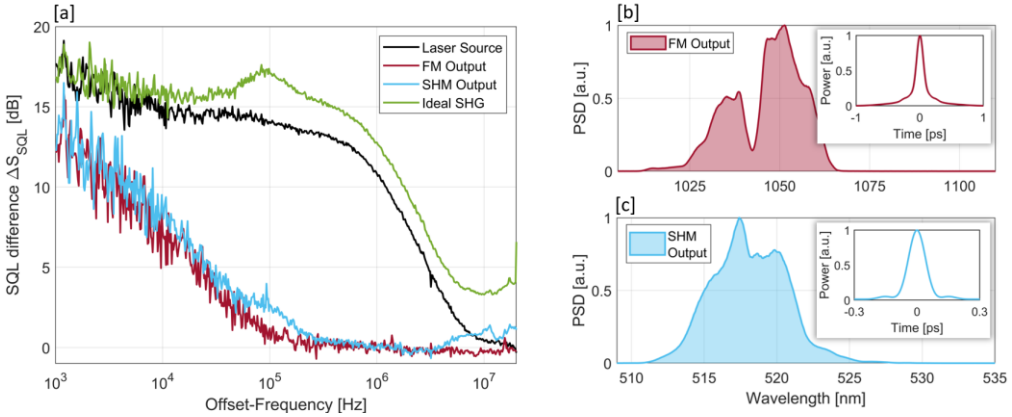

Fig. 5. [a]: Measured RIN spectral densities (1kHz-20MHz, plotted as SQL difference ΔS_{SQL}) of the laser source/LSI input (black) compared to the FM (red) and SHM (blue) system output with $\theta_{\lambda/8} = 82.5°$ and $\theta_{\lambda/2} = 160°$. The green trace shows the RIN spectrum of regular SHM with ideal phase-matching corresponding to $\theta_{\lambda/8} = \theta_{\lambda/2} = 0°$. [b]: Optical spectrum and autocorrelation trace (inset) of the FM at maximum noise suppression ($\theta_{\lambda/8} = 82.5°$). [c] Corresponding spectrum in the SHM together with the Fourier-transform limited pulse shape (inset).

Since the LSI working point with $\theta_{\lambda/8} = 85°$ and $\theta_{\lambda/2} = 160°$ seems highly promising for the generation of dual-color optical pulse trains with maximized average power and strongest noise suppression in the FM and SHM simultaneously, a closer look at the corresponding output

characteristics is justified. Fig.5 [a] shows a comparison of RIN traces measured of the laser source/LSI input and the FM and SHM system output. As an additional verification of the underlaying mechanism, Fig.5 [a] further shows the RIN trace measured in the SHM without phase-bias ($\theta_{\lambda/8} = \theta_{\lambda/2} = 0°$) and NPR, hence representing the noise transfer to the FM under ideal phase-matching and otherwise identical system parameters. As shown, the RIN spectral density of the laser source is suppressed over a broad bandwidth in both operational modes, reaching up to 14 dB in the range from 100 kHz to 1 MHz. Above 100 kHz, almost perfect SQL noise performance can be observed simultaneously in both modes with only minor distortions in the SHM. Towards lower frequencies < 100 kHz, the noise suppression becomes less efficient. In contrast, it can be seen that the regular SHG without the influence of NPR and linear polarized light parallel to the phase-matched BBO axis results in an overall amplification of the RIN spectral density compared to the laser source, in particular at higher frequencies > 10 kHz. Such RIN amplification in the phase-matched SHG process is a common phenomenon and widely reported in a variety of experimental studies [23-26]. The comparison of both cases; regular, type-I phase-matched SHG and NPR-enhanced SHG, clearly verifies the strong influence of NPR from the fiber-optic LSI as a novel underlaying mechanism for ultra-low noise SHG. Fig.5 [b] shows the FM output spectrum and the measured autocorrelation (AC) trace at the working point with maximum noise suppression in Fig.5[a]. Compared to the input spectrum of the laser source in Fig.1, the FWHM of the FM output is slightly broadened from 17 nm to ~24 nm as consequence of the nonlinear pulse propagation in the LSI. The dip at ~1042 nm can be explained with a combination of nonlinear broadening and NPR-based interaction with both the BBO and PBS1. The corresponding FWHM pulse duration is ~130 fs assuming a Gaussian pulse shape, corresponding to a FM output peak power of ~23 kW. The corresponding output spectrum of the SHM is shown in Fig.5 [c] with a FWHM of ~6 nm centered at ~518 nm. Since direct AC measurements in the SHM were not available due to practical restrictions, the inset instead shows the Fourier-transform limited pulse of the output spectrum with a FHWM of 100 fs, hence representing the ideal SHM output of the system. Under these ideal conditions, the corresponding SHM output peak power would be close to 11 kW.

4. Conclusion

In conclusion, this study introduces a novel method for ultra-low noise second harmonic generation (SHG) using Kerr-type nonlinear polarization rotation (NPR) coupled with type-I phase-matched nonlinear crystals in a nonlinear fiber interferometer. A theoretical framework is derived and successfully translated into an experimental setup, resulting in the generation of dual-color, sub-150 fs optical pulse trains at 1030 nm and 515 nm with remarkable noise reduction. Through systematic RIN measurements, our investigation reveals the system's ability to optimize local power transfer while effectively suppressing intensity noise across both fundamental and second harmonic operational modes. The achieved noise reduction, verified through frequency-resolved relative intensity noise (RIN) measurements, surpasses 14 dB for each mode. Importantly, this study demonstrates the attainment of standard-quantum limited (SQL) noise performance concurrently in both modes, indicating its potential for precision applications. Furthermore, the system exhibits significant power generation potential. At a repetition rate of 43 MHz, the SQL noise performance is correlated with average power outputs of up to 160 mW and 42 mW for the fundamental and second harmonic modes, respectively. The designed ultra-low noise dual-wavelength fiber system does not only demonstrate a novel mechanism for ultra-low noise SHG but further holds practical promise for a variety of cutting-edge applications, including multimodal two-photon microscopy, ultra-low noise seeding of parametric down-conversion in quantum communication and information processing, nonlinear laser spectroscopy, frequency comb generation, and fiber-optic sensing.

Funding. This work has been supported by Deutsches Elektronen-Synchrotron DESY, a member of the Helmholtz Association (HGF), POF IV DMC and the Cluster of Excellence 'Advanced Imaging of Matter' of the Deutsche Forschungsgemeinschaft (DFG) – EXC 2056 – project ID 390715994.

Disclosures. The authors declare no conflicts of interest.

Data availability. Data underlaying the results presented in this paper are not publicly available at this time but may be obtained by the authors upon reasonable request.

References

1. C. A. Casacio, L. S. Madsen, A. Terrasson, M. Waleed, K. Barnscheidt, B. Hage, M. A. Taylor, and W. P. Bowen, "Quantum-enhanced nonlinear microscopy," Nature 594, 201–206 (2021).
2. X. Xie, R. Bouchand, D. Nicolodi, M. Giunta, W. Hänsel, M. Lezius, A. Joshi, S. Datta, C. Alexandre, and M. Lours, "Photonic microwave signals with zeptosecond-level absolute timing noise," Nat. Photonics 11, 44–47 (2017).
3. T. Udem, R. Holzwarth, and T. W. Hänsch, "Optical frequency metrology," Nature 416, 233–237 (2002).
4. S. T. Cundiff and A. M. Weiner, "Optical arbitrary waveform generation," Nat. Photonics 4, 760–766 (2010).
5. W. Hänsel, H. Hoogland, M. Giunta, S. Schmid, T. Steinmetz, R. Doubek, P. Mayer, S. Dobner, C. Cleff, M. Fischer, and R. Holzwarth, "All polarization-maintaining fiber laser architecture for robust femtosecond pulse generation," *Appl. Phys. B* 123, 41 (2017).
6. Y. Ma, S. H. Salman, C. Li, C. Mahnke, Y. Hua, S. Droste, J. Fellinger, A. S. Mayer, O. H. Heckl, C. M. Heyl, and I. Hartl, "Compact, All-PM Fiber Integrated and Alignment-Free Ultrafast Yb:Fiber NALM Laser With Sub-Femtosecond Timing Jitter," *J. Lightwave Technol. 39*, 4431-4438 (2021).
7. D. Kim, D. Kwon, B. Lee, and J. Kim, "Polarization-maintaining nonlinear-amplifying-loop-mirror mode-locked fiber laser based on a 3 × 3 coupler," *Opt. Lett.* 44, 1068-1071 (2019).
8. J. Szczepanek, T. M. Kardaś, M. Michalska, C. Radzewicz, and Y. Stepanenko, "Simple all-PM fiber laser mode-locked with a nonlinear loop mirror," *Opt. Lett.* 40, 3500-3503 (2015).
9. X. Liu, R. Zhou, D. Pan, Q. Li, and H. Y. Fu, "115-MHz Linear NPE fiber laser using all polarization-maintaining fibers," *IEEE Photonics Technol. Lett.* 33, 81–84 (2021).
10. G. Liu, S. Ou, Q. Zhang, M. Zhang, X. Li, and Q. Bao, "All-polarization-maintaining linear fiber laser mode-locked by nonlinear polarization evolution with phase bias," *Opt. Laser Technol.* 142, 107160 (2021).
11. M. E. Fermann, L.-M. Yang, M. L. Stock, and M. J. Andrejco, "Environmentally stable Kerr-type mode-locked erbium fiber laser producing 360-fs pulses," *Opt. Lett.* 19, 43-45 (1994).
12. N. Kuse, J. Jiang, C.-C. Lee, T. R. Schibli, and M.E. Fermann, "All polarization-maintaining Er fiber-based optical frequency combs with nonlinear amplifying loop mirror," *Opt. Express* 24, 3095-3102 (2016).
13. Y. Pi, H. Tian, R. Li, Y. Han, Y. Song, and M. Hu, "Timing jitter and intensity noise characterization of a 122-MHz all-PM NALM mode-locked fiber laser," *IEEE Photonics Technol. Lett.* 33, 1439–1442 (2021).
14. K.Yang, L. Feng, K. Wei, C. Liu, H. Zhu, C. Guo, P. Yan, S. Ruan, and J. Wang, "All-polarization-maintaining NALM mode-locked Er/Yb-doped large-mode-area fiber oscillator," *Opt. Lett.* 47, 4893-4896 (2022).
15. W. Liu, H. Shi, J. Cui, C. Xie, Y. Song, C. Wang, and M. Hu, "Single-polarization large-mode-area fiber laser mode-locked with a nonlinear amplifying loop mirror," *Opt. Lett.* 43, 2848–2851 (2018).
16. M. Edelmann, M. M. Sedigheh, Y. Hua, E. C. Vargas, M. Pergament, and F. X. Kärtner, "Large-mode-area soliton fiber oscillator mode-locked using NPE in an all-PM self-stabilized interferometer," *Appl. Opt.* 62, 1672-1676 (2023).
17. E. S. Lamb, L. G. Wright, and F. W. Wise, "Divided-pulse lasers," *Opt. Lett.* 39, 2775-2777 (2014).
18. M. Edelmann, Y. Hua, G. Kulcsar, and F. X. Kärtner, "All-polarization-maintaining divided pulse fiber oscillator mode-locked with the optical Kerr effect," *Opt. Lett*. 46, 6083-6086 (2021).
19. M. Edelmann, Y. Hua, K. Şafak, and F. X. Kärtner, "Nonlinear fiber system for shot-noise limited intensity noise suppression and amplification," *Opt. Lett.* 46, 3344-3347 (2021).
20. G. Dai, and Y. Ozeki. "All-fiber polarization-maintaining system for noise suppression and signal amplification of picosecond pulses." *Japanese Journal of Appl. Phys.* 61, 080905 (2022).
21. Z. Tang, D. Luo, L. Zhou, G. Xie, C. Gu, Z.Deng, S. Xiong, Y. Liu, and W. Li "Passive noise suppression in Yb-doped fiber amplifier based on nonlinear amplifying loop mirror." *Optics & Laser Technology* 160, 109088 (2023).
22. A. Casanova, Q. D'Acremont, G. Santarelli, S. Dilhaire, and A. Courjaud, "Ultrafast amplifier additive timing jitter characterization and control," *Opt. Lett.* 41, 898-900 (2016).
23. V. Silva de Oliveira, A. Ruehl, P. Masłowski, and I. Hartl, "Intensity noise optimization of a mid-infrared frequency comb difference-frequency generation source," *Opt. Lett.* 45, 1914-1917 (2020).
24. M. Huber, W. Schweinberger, F. Stutzki, J. Limpert, I. Pupeza, and O. Pronin, „ Active intensity noise suppression for a broadband mid-infrared laser source," *Opt. Express* 25, 22499-22509 (2017).
25. R. Yang, M. Zhao, X. Jin, Q. Li, Z. Chen, A. Wang, and Z. Zhang, "Attosecond timing jitter from high repetition rate femtosecond "solid-state fiber lasers"," *Optica* 9, 874-877 (2022).
26. M. Laçin, P. Repgen, A. Şura, Ç Şenel, and F. Ö. Ilday, "Analogy of harmonic modelocked pulses to trapped Brownian particles improves laser performance," *Appl. Phys. B* 129, 46 (2023).

27. D. K. Serkland, P. Kumar, M. A. Arbore, and M. M. Fejer, „Amplitude squeezing by means of quasi-phase-matched second-harmonic generation in a lithium niobate waveguide," *Opt. Lett.* 22, 1497-1499 (1997).
28. Y. Li, D. Guzun, and M. Xiao, "Quantum-noise measurements in high-efficiency single-pass second-harmonic generation with femtosecond pulses," *Opt. Lett.* 24, 987-989 (1999).
29. T. C. Ralph, M. S. Taubman, A. G. White, D. E. McClelland, and H.-A. Bachor, "Squeezed light from second-harmonic generation: experiment versus theory," *Opt. Lett.* 20, 1316-1318 (1995).
30. R. D. Li, and P. Kumar, "Quantum-noise reduction in traveling-wave second-harmonic generation," *Phys. Rev. A* 49, 2157 (1994).
31. N. Almat, W. Moreno, M. Pellaton, F. Gruet, C. Affolderbach, and G. Mileti, "Characterization of Frequency-Doubled 1.5-µm Lasers for High-Performance Rb Clocks," *IEEE Trans. Ultrason. Ferroelectr. Freq. Control.* 65, 919 (2018).
32. X. Zeng, S. Cui, J. Qian, X. Cheng, J. Dong, J. Zhou, Z. Xu, and Y. Feng, "10 W low-noise green laser generation by the single-pass frequency doubling of a single-frequency fiber amplifier," *Laser Phys.* 30, 075001 (2020).
33. C. Dixneuf, G. Guiraud, H. Ye, Y. Bardin, M. Goeppner, G. Santarelli, and N. Traynor, "Robust 17 W single-pass second-harmonic-generation at 532 nm and relative-intensity-noise investigation," *Opt. Lett.* 46, 408-411 (2021).
34. R. Collin, T. Chartier, and P. Besnard, "Numerical investigation of relative intensity noise in frequency-doubled multimode fiber lasers," *Opt. Commun. 485*, 126724 (2021).
35. M. Tawfieq, A. K. Hansen, O. B. Jensen, D. Marti, B. Sumpf and P. E. Andersen, "Intensity Noise Transfer Through a Diode-Pumped Titanium Sapphire Laser System," *IEEE J. Quantum Electron.* 54, 1-9 (2018).
36. Z. Łaszczych, M. Krakowski, and G. Soboń, "Mode-Locking Dynamics in an All-PM Figure-Nine Tm-Doped Fiber Laser," *Appl. Sci.* 12, 10613 (2022).
37. S. Peng, X. Liu, H. Y. Fu, and Q. Li, "Intracavity filtering effect in a dual-output linear-cavity all-PM fiber laser mode-locked by NPE," *Appl. Opt.* 62, 6323-6332 (2023).
38. X. Liu, F. Ye, M. Zhao, B. A. Malomed, H. Y. Fu and Q. Li, "All-Polarization-Maintaining Linear Cavity Fiber Lasers Mode-Locked by Nonlinear Polarization Evolution in Stretched Pulse Regime," *J. Lightwave Technol.* 41, 5107-5115 (2023).
39. M. E. Fermann, F. Haberl, M. Hofer, and H. Hochreiter, "Nonlinear amplifying loop mirror," *Opt. Lett.* 15, 752-754 (1990).
40. M. Edelmann, Y. Hua, K. Şafak, and F. X. Kärtner, "Intrinsic amplitude-noise suppression in fiber lasers mode-locked with nonlinear amplifying loop mirrors," *Opt. Lett.* 46, 1752-1755 (2021).
41. M. Edelmann, M. Pergament, and F. X. Kärtner. "Intra-Pulse Intensity Noise Shaping by Saturable Absorbers." arXiv preprint arXiv:2303.13420 (2023).